

## Research Article

# Numerical Simulation of Air Entrainment Performance of a Foam Generator Used for Dust Control in Coal Mines

Hetang Wang <sup>1,2</sup> and Yan Tang <sup>3</sup>

<sup>1</sup>State Key Laboratory of Coal Resources and Safe Mining, China University of Mining and Technology, Xuzhou 221116, China

<sup>2</sup>School of Safety Engineering, China University of Mining and Technology, Xuzhou 221116, China

<sup>3</sup>School of Environmental and Safety Engineering, Changzhou University, Changzhou 213164, China

Correspondence should be addressed to Hetang Wang; wanghetang@cumt.edu.cn

Received 27 February 2019; Revised 10 June 2019; Accepted 1 July 2019; Published 4 August 2019

Academic Editor: Adrian Chmielewski

Copyright © 2019 Hetang Wang and Yan Tang. This is an open access article distributed under the Creative Commons Attribution License, which permits unrestricted use, distribution, and reproduction in any medium, provided the original work is properly cited.

Mine dust is one of the most serious environmental hazards in the coal mining process. This paper introduces a numerical simulation of a novel foam generator used for dust control in coal mines. The amount of foam generated by this device significantly depends on the amount of air entrainment. Therefore, a computational fluid dynamics (CFD) method was used to study three influencing factors, namely, throat-nozzle distance, mixing throat length, and the contraction angle of the suction chamber. The predicted values by the CFD simulation proved to be in good agreement with the experimental data. The results revealed that the air entrainment reached its maximum when the ratio of throat-nozzle distance to mixing throat length was 2/3. The optimum values of the throat ratio (its length to diameter) and the contraction angle of the suction chamber were obtained at 20 and 5°, respectively. This research provides essential guidance in the geometric parameter design of the self-suction type foam generator, which has the advantage of negating the need for compressed-air pipelines and having high reliability, compared to traditional foam generators.

## 1. Introduction

Mine dust is one of the most serious hazards in coal mines; it severely pollutes the air in underground working environments [1, 2], leads to dust explosions and coal workers' pneumoconiosis (CWP), and thus can result in casualties and economic loss in coal mines [3–5]. Among the 18 major coal-mine accidents recorded worldwide, each resulting in over 300 deaths, 16 were caused by dust or dust-methane explosions [6]. CWP is a global occupational disease existing in nearly all major coal-mining countries. In the USA, 8% of the workers who served in underground coal mines for over 25 years were diagnosed with CWP; 69,337 workers died because of CWP during the period 1970-2004 [7]. Thus, there is an urgent need for the development and application of an efficient dust suppression technology.

There are various technologies for mine dust control, such as water sprays [8–12], air-curtains [13, 14], dust collectors [15], wetting agents (surfactants) [16, 17], and foams [18, 19]. Among them, foam technology plays an extremely significant role. Compared with water mist, foam has a larger surface

area and stronger ability in dust adhesion and wetting [20, 21]. In particular, foam has a higher efficiency in suppressing respirable dust with small diameters [6, 18]. Hence, foam technology has been widely investigated and adopted in mine dust control. The production of foam is to the core of foam technologies. Almost all foam generators produce foam with compressed air; however this presents some common shortcomings: (a) extra compressed air pipelines need to be paved, taking up a lot of space and increasing the complexity of the system; (b) higher costs due to the large consumption of water and foaming agent; (c) backflow of pressure water which cannot be adjusted easily due to the pressure energy of compressed air being so strong. In order to overcome such drawbacks, a novel foam generator with air self-suction has been developed [22]. In this generator, the pressurized water is the power and used as the driven fluid, and the air and foaming agent are automatically sucked into the induction chamber by the negative pressure formed by the water jet. The water, air, and foaming agent are mixed in the mixing chamber, producing the primary foam, which will be enhanced by the swirler in the foaming chamber.

This foam generator with air-suction was shown to achieve positive dust suppression effect in field applications [23]. The suction performance of foaming agent was also investigated at length [24]. However, it is evident that there is still a lack of in-depth studies on the relationship between the air entrainment performance and the geometric parameters of this foam generator. This has hindered the high volume and low cost production of dust-suppression foam, since the foam production quantities significantly depend on the air entrainment performance of the foam generator.

Therefore, in order to get the optimum geometric parameters with which the air entrainment of the foam generator would be maximum, three influencing factors of air entrainment were investigated, namely, throat-nozzle distance, mixing throat length, and contraction angle of the suction chamber (or induction chamber). Two dimensionless parameters were used in the study, the ratio  $R_{td}$  (throat-nozzle distance to mixing throat length) and the ratio  $R_{ld}$  (the throat's length to its diameter). A computational fluid dynamics (CFD) method was adopted due to the simulation's lower-cost, reliability, and ease of use [25–27].

## 2. Simulation Methods

**2.1. Mathematical Model.** The progress of jet suction in the foam generator can be classified into a gas-liquid two-phase flow (in this paper, the suction of the foaming agent was not studied as the amount of air entrainment was the main influencing factor contributing to foam generation). There are two methods for the numerical calculation of multiphase flows: the Euler-Lagrange method and the Euler-Euler method [28]. In the Euler-Lagrange method, a particle is taken as the research object and the particle trajectory equations are solved in the Lagrangian framework, whilst in the Euler-Euler method, different phases are treated as interpenetrating continua which is more suitable for the jet suction process used in this paper. As the control equations for air and water are similar, water phase is taken as the example and its control equations are detailed as follows [29, 30].

The continuity equation:

$$\frac{\partial}{\partial t} (\alpha_0 \rho_0) + \nabla \cdot (\alpha_0 \rho_0 \vec{u}_0) = \dot{m}_{g0} - \dot{m}_{0g} \quad (1)$$

where  $\alpha_0$  represents the fraction of water volume and  $\vec{u}_0$  is the velocity of the phase water,  $\rho_0$  is the density of water,  $\dot{m}_{g0}$  characterizes the mass transfer from gas to water, and  $\dot{m}_{0g}$  characterizes the mass transfer from water to gas.

The conservation of momentum equation:

$$\begin{aligned} & \frac{\partial}{\partial t} (\alpha_0 \rho_0 \vec{u}_0) + \nabla \cdot (\alpha_0 \rho_0 \vec{u}_0 \vec{u}_0) \\ &= -\alpha_0 \nabla p + \nabla \cdot \vec{\tau}_0 + \alpha_0 \rho_0 \vec{g} \\ &+ \left( \vec{R}_{g0} + \dot{m}_{g0} \vec{u}_{g0} - \dot{m}_{0g} \vec{u}_{0g} \right) \\ &+ \left( \vec{F}_0 + \vec{F}_{lift,0} + \vec{F}_{m,0} \right) \end{aligned} \quad (2)$$

where  $\vec{\tau}_0$  is the stress-strain tensor of water,  $\vec{F}_0$  is an external body force,  $\vec{F}_{lift,0}$  is a lift force,  $\vec{F}_{m,0}$  is a virtual mass force,  $\vec{R}_{g0}$  is an interaction force between phases, and  $p$  is the pressure shared by two phases.

The energy conservation equation:

$$\begin{aligned} & \frac{\partial}{\partial t} (\alpha_0 \rho_0 h_0) + \nabla \cdot (\alpha_0 \rho_0 \vec{u}_0 h_0) \\ &= \alpha_0 \frac{\partial p_0}{\partial t} + \nabla \vec{u}_0 \cdot \vec{\tau}_0 - \nabla \cdot \vec{q}_0 + S_0 + Q_{0g} + \dot{m}_{g0} h_{g0} \\ & - \dot{m}_{0g} h_{0g} \end{aligned} \quad (3)$$

where  $h_0$  is the specific enthalpy of water phase,  $\vec{q}_0$  is the heat flux,  $S_0$  is the source item that contains the enthalpy,  $Q_{0g}$  is the strength of heat conduction between water and air, and  $h_{g0}$  is the enthalpy value of the interphase.

The Realizable k-epsilon model is employed to model the turbulent behavior of flow in the generator.

**2.2. Geometric Model.** The geometric model was established using CAD and Gambit software. Subsequently, meshes were generated and the boundary conditions were set.

In the meshing process, the suction chamber was separated from the whole model and meshed with denser, unstructured ‘‘Tgrid’’ elements which have strong adaptability, whilst the other chambers were meshed with the ‘‘Hex/Wedge’’ elements. The total number of the grids varied as the structure parameters changed in different models. For instance, when the throat-nozzle distance was 12 mm, the mixing throat length was 360 mm and the contraction angle of the suction chamber was 20° and the total number of mesh elements was 219617, among which the number of the suction chamber was 74277.

Figure 1 shows the boundary conditions of the model. The pressurized water jet can be considered as incompressible fluid flow. Thus the velocity inlet was taken as the boundary condition for the flow of water when the volumetric flow rate of water at the nozzle was fixed. The air inlet was set as the pressure inlet whilst the ejector outlet was considered the pressure outlet. Their gauge pressures were considered to be 0 Pa since they were both open to atmosphere. The solution was initialized by taking the ejector geometry as being completely filled with air.

**2.3. Solution Method.** The calculations were conducted on an AMD6272 server (128 CPU core, 2.1 GHz dominant frequency and 256G internal storage) with FLUENT 14.5 software. The simulation process was divided into three steps: (a) simulation of air entrainment under different throat-nozzle distances; (b) simulation of air entrainment under different lengths of mixing throat; (c) simulation of air entrainment under different contraction angles of the suction chamber.

## 3. Results and Discussion

The foam generator studied in this paper is essentially a special jet pump which can safely and reliably mix several

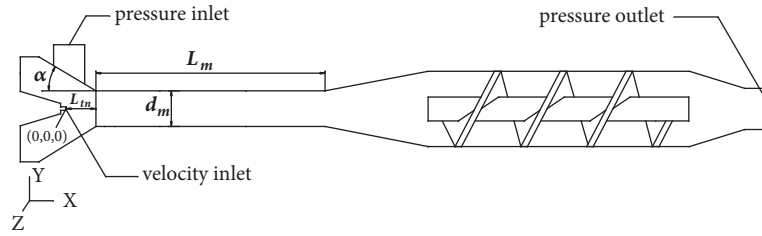


FIGURE 1: Schematic diagram of boundary conditions setting:  $\alpha$  contraction angle of suction chamber;  $L_m$  length of throat;  $d_m$  diameter of throat;  $L_{tn}$  throat-nozzle distance.

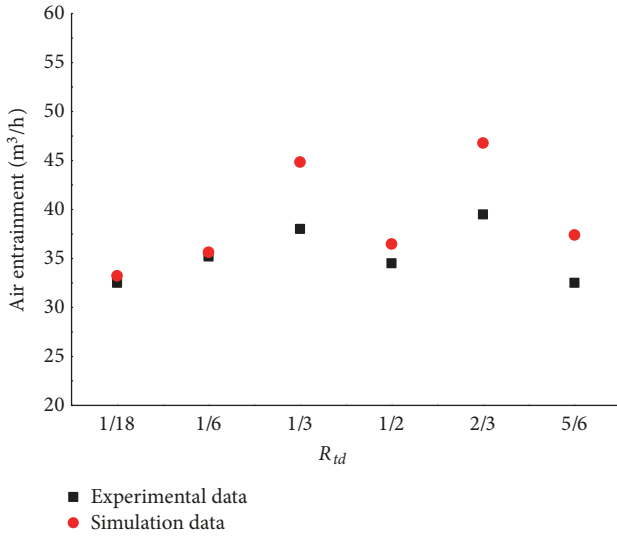


FIGURE 2: Simulation and experimental data of air entrainment under different  $R_{td}$ .

kinds of material. Based on the design theory of a jet pump, throat-nozzle distance, mixing throat length, and contraction angle are important structural parameters affecting the suction performance [31–35]. Thus, this paper chose these parameters as a measure of the performance of the foam generator.

**3.1. Validation of Model.** In order to validate the model and obtain high accuracy of the simulation results, related experiments were undertaken to compare the simulation results with measured results by using the experimental setup in [22]. Figure 2 shows the comparison between the simulation values and the experimental data for air entrainment under different  $R_{td}$  values. The throat length and the contraction angle were set at 360 mm and  $20^\circ$ , respectively (with a jet velocity of 89.75 m/s). It can be seen from Figure 2 that the simulation and experimental values showed similar variation trends and good agreement overall. Attributing reasons for errors between the experimental and simulation data include the following: (a) the control equations used in FLUENT software are applicable to the general situation but may not be totally accurate to the specific problem presented in this paper; (b) the sensors used in the experiments may have inaccuracies/sensitivities and their locations may not have

been the most appropriate; (c) the initial conditions (such as the turbulence intensity) are time-averaged in the simulation but are distributed unevenly in reality. Taking all of these aspects into consideration, the simulation results can be considered credible.

**3.2. The Effect of Throat-Nozzle Distance on Air Entrainment.** The throat length and the contraction angle of the suction chamber were set at 360 mm and  $20^\circ$ , respectively. The throat-nozzle distance was viewed as a variable and the simulations were conducted under the values of 1.0 mm, 3.0 mm, 6.0 mm, 9.0 mm, 12.0 mm, and 15.0 mm. As the throat diameter  $d_m$  was 18 mm, the ratio ( $R_{td}$ ) of throat-nozzle distance to mixing throat length was thus 1/18, 1/6, 1/3, 1/2, 2/3, and 5/6, respectively. There were 8 different values of jet velocity  $v_n$  under each ratio, 52.97 m/s, 55.96 m/s, 65.55 m/s, 75.13 m/s, 83.94 m/s, 89.75 m/s, 96.51 m/s, and 104.22 m/s.

Figure 3 shows the velocity nephogram of the water and air phases on section  $Z=0$ mm when  $v_n$  is 104.22 m/s and  $R_{td}$  is 2/3. As water ejects from the nozzle at high velocity, the outside air is induced into the suction chamber and moves together with the water.

Figure 4 shows the air entrainment  $Q_g$  under different  $R_{td}$  values. For each  $v_n$ , the air entrainment was highest when the  $R_{td}$  was 2/3 and decreased to its lowest point when the  $R_{td}$  was 1/18. As the  $R_{td}$  transitioned from 1/18 to 1/3, the air entrainment showed an increase and reached a high point when the  $R_{td}$  was 1/3. With a jet velocity of 83.94m/s and  $R_{td}$  at 1/3,  $Q_g$  was 1.49 times greater than that when  $R_{td}$  was at 1/18. As  $R_{td}$  increased from 1/3 to 2/3, air entrainment first decreased, then raised, and reached the peak when  $R_{td}$  was 2/3. Furthermore, the air entrainment showed a decreasing trend as  $R_{td}$  increased from 2/3 to 5/6. Thus for this device, the optimal value for  $R_{td}$  was found to be 2/3; hence, the optimal throat-nozzle distance was 12 mm when the throat length was 18 mm.

**3.3. The Effect of the Length of Throat on Air Entrainment.** The throat-nozzle distance and contraction angle of the suction chamber were set to a value of 12mm and  $20^\circ$ , respectively, and the simulations were conducted under different mixing throat lengths of the 540mm, 450 mm, 360 mm, 270 mm, and 180 mm. The ratios for  $R_{td}$  (the length to diameter of throat) were 35, 30, 25, 20, 15, and 10 respectively. Furthermore, there were 8 values of jet velocity  $v_n$  tested under each ratio: 47.79 m/s, 50.77 m/s, 56.75 m/s, 65.71 m/s, 77.18 m/s, 85.83 m/s, 94.00 m/s, and 102.18 m/s.

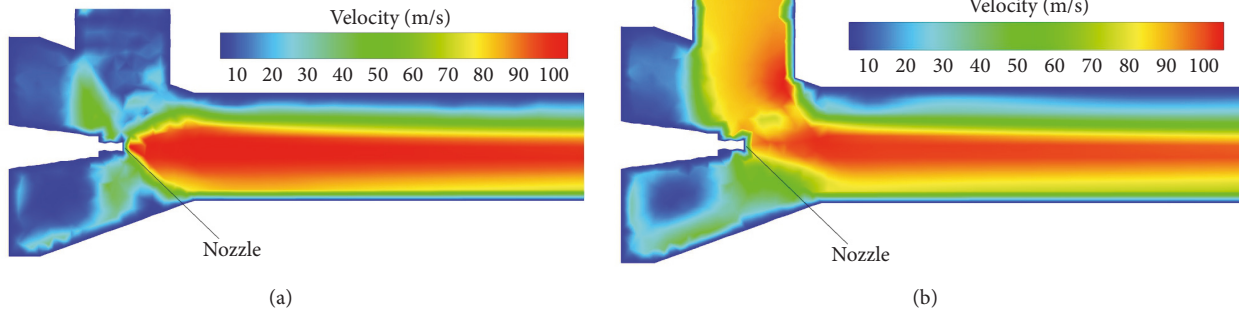


FIGURE 3: Velocity nephogram of (a) water phase and (b) air phase on section  $Z=0$  mm when  $v_n$  is 104.22 m/s and  $R_{td}$  is 2/3.

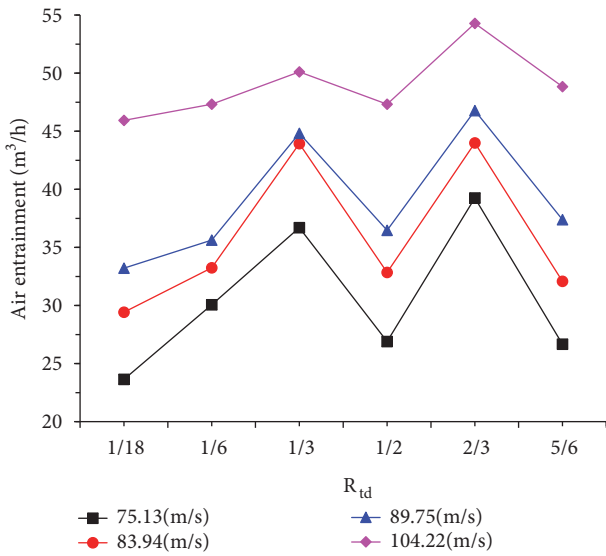


FIGURE 4: Change of  $Q_g$  with  $R_{td}$  when the  $L_m$  and  $\alpha$  are 360 mm and  $20^\circ$ , respectively.

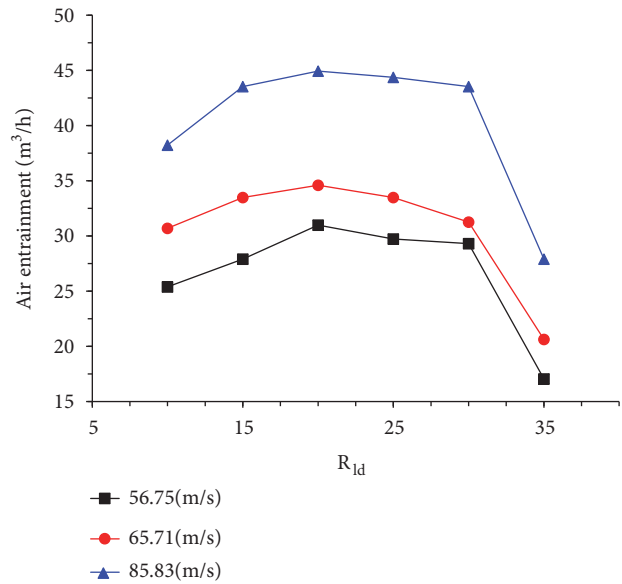


FIGURE 5: Change of  $Q_g$  with  $R_{td}$  when  $L_m$  and  $\alpha$  are 12mm and  $20^\circ$ , respectively.

Figure 5 shows the changes in air entrainment  $Q_g$  under 6 different values of  $R_{td}$ . As illustrated in the figure, the air entrainment reaches its highest point when  $R_{td}$  is 20 and falls to its lowest point when the  $R_{td}$  is 35. As  $R_{td}$  increases from 10 to 20, the air entrainment shows a corresponding increase and reaches a peak when the  $R_{td}$  is 20. As  $R_{td}$  increases from 20 to 30, air entrainment experiences a slow decrease, and then it falls significantly when  $R_{td}$  is 35. With a jet velocity of 65.71m/s, the minimum value of air entrainment decreases by 41% as compared to peak values. Thus for this device, the optimal value of  $R_{td}$  was found to be 20, with the optimal throat length of 360 mm and throat diameter of 18 mm.

**3.4. The Effect of the Contraction Angle on Air Entrainment.** The throat-nozzle distance and throat length were set with values of 12mm and 360mm, respectively, and simulations were conducted under different contraction angles  $\alpha$  of  $3^\circ$ ,  $5^\circ$ ,  $10^\circ$ ,  $15^\circ$ ,  $20^\circ$ ,  $25^\circ$ ,  $45^\circ$ , and  $60^\circ$ . There were 8 values for the jet velocity  $v_n$  under each  $\alpha$ : 45.00 m/s, 55.96 m/s, 65.55 m/s, 75.13 m/s, 83.94 m/s, 89.75 m/s, 96.51 m/s, and 104.22 m/s.

Figure 6 shows the air entrainment  $Q_g$  under 8 different contraction angles of the suction chamber. The air entrainment reached its highest point when  $\alpha$  was at  $5^\circ$  and fell to its lowest point when  $\alpha$  was  $60^\circ$ . When  $\alpha$  increased from  $3^\circ$  to  $5^\circ$ , the air entrainment showed a slight increase. As  $\alpha$  increases from  $5^\circ$  to  $20^\circ$ , the air entrainment decreased. The air entrainment remained relatively steady when  $\alpha$  varied from  $20^\circ$  to  $45^\circ$ , after which it dropped dramatically when  $\alpha$  was  $60^\circ$ . With respect to the jet velocity of 89.75m/s, the air entrainment decreased by 39.4% and was only 60% of maximum values.

Since the secondary fluid air is induced by the negative pressure generated by the jet, the effect of  $\alpha$  can be explained by the driving force of negative pressure in the chamber. Figure 7 shows the pressure cloud chart of the suction chamber on section  $Y=0$  mm and  $Z=0$  mm. The jet velocity was 77.18 m/s, the contraction angle of the suction chamber was  $20^\circ$ , throat length was 450 mm, and the throat-nozzle distance was 12mm. The high negative pressure mainly existed in the area around the nozzle exit and the entrance of mixing chamber.

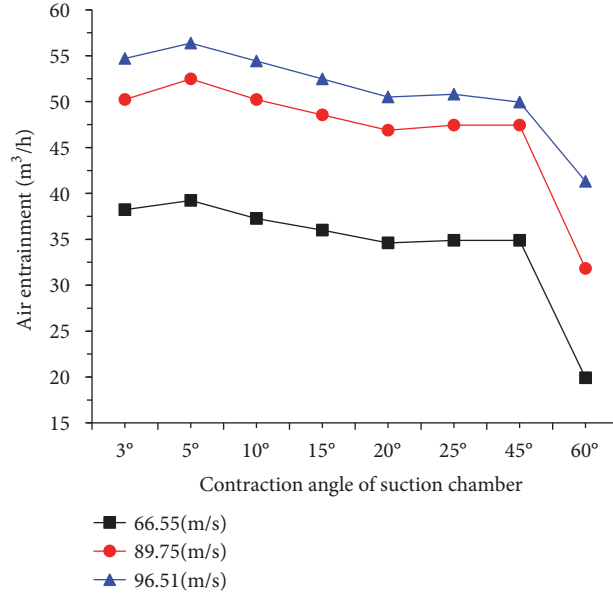


FIGURE 6: Change of  $Q_g$  with  $\alpha$  when  $L_{tn}$  and  $L_m$  are 12mm and 360mm, respectively.

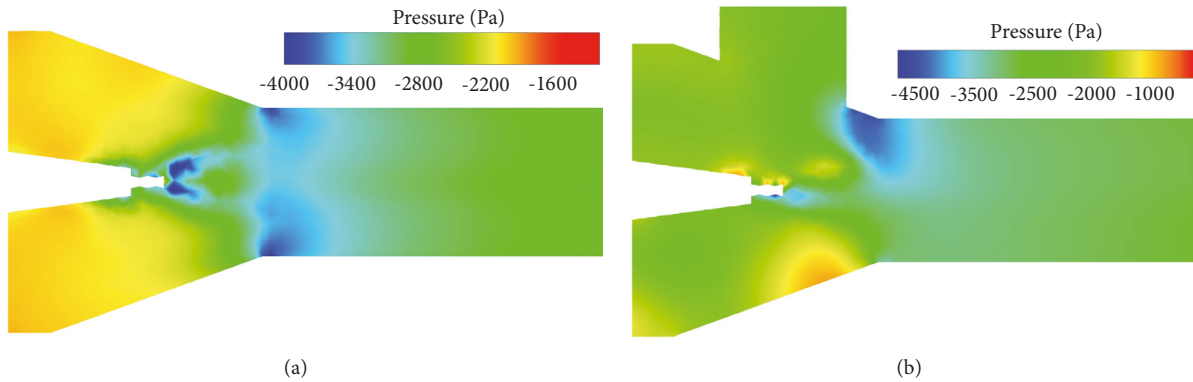


FIGURE 7: Pressure distribution nephogram on section (a)  $Y=0\text{mm}$  and (b)  $Z=0\text{mm}$ .

Figure 8 describes the static pressure values along the central axis which begin from the nozzle exit with a jet velocity of 96.51 m/s and  $\alpha$  value of 20°. The static pressure first decreased sharply and then increased rapidly until it is about 5 mm from the nozzle exit and reached the minimum point at a value of -6200 Pa. Subsequently, the static pressure went through a fluctuation phase which was not as intense. This result was consistent with the phenomenon of shock train in ejectors which is driven by the combined effect of interphase drag and turbulent eddies [36]. In this case, the vacuum degree, which is the absolute value of negative pressure, was used to describe the strength of the negative pressure; correspondingly, the maximum vacuum degree is 6200 Pa.

Figure 9 indicates the maximum vacuum degrees along the central axis under different contraction angles. The maximum vacuum degree was highest when  $\alpha$  was 5° and fell to its lowest point when  $\alpha$  was 60°. As  $\alpha$  increased from 3° to 5°, the maximum vacuum degree increased and

reached a peak when  $\alpha$  was 5°. The maximum vacuum degree exhibited a tendency to decrease as  $\alpha$  increased from 5° to 60°. Therefore, the optimal value of  $\alpha$  was 5° which illustrated a corresponding larger vacuum degree.

In conjunction with Figure 6, a synchronous variation can be found between the vacuum degree and the air entrainment. This phenomenon can be explained by the following equation which indicates that for the determined parameters, the air entrainment  $Q_g$  increases with the vacuum degree in the suction chamber [22]:

$$Q_g = \frac{\pi d_a^2}{4} \times \frac{\sqrt{2(p_{atm} - p_m) / \rho_g}}{\sqrt{\mu_1 + \mu_2 + kd_a^4 / d_m^4}} \quad (4)$$

where  $d_m$  is the throat diameter;  $d_a$  is the diameter of air suction hole;  $\rho_g$  is air density,  $\text{kg/m}^3$ ;  $p_{atm}$  and  $p_m$  denote the atmospheric pressure and air pressure, respectively, at the

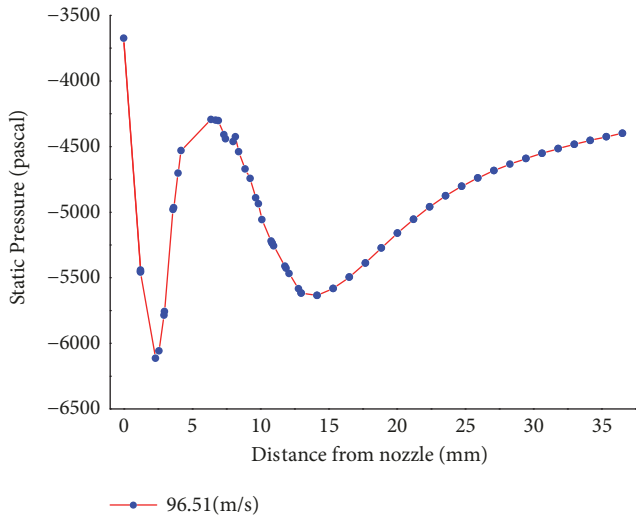


FIGURE 8: Static pressure on central X axis.

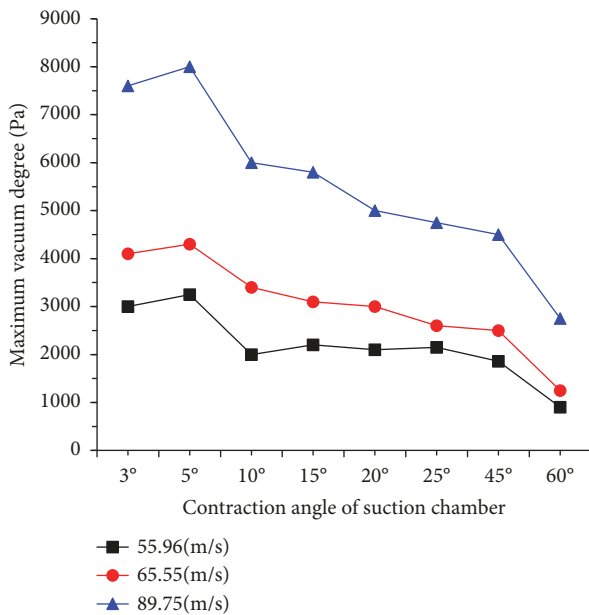


FIGURE 9: Change of maximum vacuum degree with  $\alpha$ .

throat inlet, MPa;  $\mu_1$  and  $\mu_2$  denote the local resistance coefficient at the inlet and outlet of the suction hole, respectively;  $k$  is the kinetic energy correction coefficient of the throat section.

**3.5. Field Application.** With adoption of the parameters mentioned above, this foam generator with air self-suction can have good foam-production ability and high dust-suppression efficiency in field applications and have been utilized in several coal mines in the Huaibei mining area such as Zhuxianzhuang Coal Mine [22, 23].

## 4. Conclusions

The air entrainment performance of the foam generator presented in this paper was shown to be significantly affected

by the ratio of the throat-nozzle distance to the mixing throat length ( $R_{td}$ ), the length-diameter ratio of the mixing throat ( $R_{ld}$ ), and the contraction angle of the suction chamber ( $\alpha$ ). The following conclusions are presented.

- (1) The foam generator's air entrainment reaches a peak when the  $R_{td}$  is 1/3 and 2/3. The minimum and maximum values for air entrainment are obtained when  $R_{td}$  is 1/18 and 2/3, respectively. With the optimal value of  $R_{td}$  at 2/3 in this paper, the optimal throat-nozzle distance is 12 mm when the throat length is 18 mm.
- (2) Raising the length-diameter ratio,  $R_{ld}$ , increases the amount of air suction initially but this begins to decrease after surpassing a certain value. The maximum and minimum values of air entrainment are obtained when  $R_{ld}$  is 20 and 35, respectively. Hence, the optimal value of  $R_{ld}$  is 20, with the optimal throat length at 360 mm, when the diameter of throat is 18 mm.
- (3) As the contraction angle of the suction chamber ( $\alpha$ ) increases from  $3^\circ$  to  $60^\circ$ , the air entrainment shows a trend of increasing initially and subsequently decreasing after surpassing a specific value. A peak value is obtained when  $\alpha$  is  $5^\circ$  and this falls significantly when  $\alpha$  is  $60^\circ$ . Thus, the optimal value of  $\alpha$  for the device is  $5^\circ$ .
- (4) The optimum parameters have a corresponding larger vacuum degree. Thus, there is a positive relationship between the vacuum degree and the air entrainment.

## Data Availability

The data used to support the findings of this study are included within the article.

## Conflicts of Interest

The authors declare that they have no conflicts of interest.

## Acknowledgments

This work was supported by the China Postdoctoral Science Foundation funded project (2018T110574), the Independent Research Project of State Key Laboratory of Coal Resources and Safe Mining, CUMT (SKLCSRSM19X004), and the Jiangsu Planned Projects for Postdoctoral Research Funds (1601234C).

## References

- [1] Q. Zhang, G. Zhou, X. Qian, M. Yuan, Y. Sun, and D. Wang, "Diffuse pollution characteristics of respirable dust in fully-mechanized mining face under various velocities based on CFD investigation," *Journal of Cleaner Production*, vol. 184, pp. 239–250, 2018.
- [2] P. Cai, W. Nie, D. Chen, S. Yang, and Z. Liu, "Effect of air flow rate on pollutant dispersion pattern of coal dust particles at fully mechanized mining face based on numerical simulation," *Fuel*, vol. 239, pp. 623–635, 2019.

- [3] V. Ebadat, "Dust explosion hazard assessment," *Journal of Loss Prevention in the Process Industries*, vol. 23, no. 6, pp. 907–912, 2010.
- [4] J. F. Hurley, J. Burns, L. Copland, J. Dodgson, and M. Jacobsen, "Coalworkers' simple pneumoconiosis and exposure to dust at 10 British coalmines," *British Journal of Industrial Medicine*, vol. 39, no. 2, pp. 120–127, 1982.
- [5] Y.-P. Zheng, C.-G. Feng, G.-X. Jing et al., "A statistical analysis of coal mine accidents caused by coal dust explosions in China," *Journal of Loss Prevention in the Process Industries*, vol. 22, no. 4, pp. 528–532, 2009.
- [6] D. M. Wang, *Mine Dusts*, Science Press, Beijing, China, 2015.
- [7] J. F. Colinet, *Best Practices for Dust Control in Coal Mining*, US Department of Human Health Services, Pittsburgh, Pa, USA, 2010.
- [8] J. Wang, G. Zhou, X. Wei, and S. Wang, "Experimental characterization of multi-nozzle atomization interference for dust reduction between hydraulic supports at a fully mechanized coal mining face," *Environmental Science and Pollution Research*, vol. 26, no. 10, pp. 10023–10036, 2019.
- [9] P. Wang, C. Tian, R. Liu, and J. Wang, "Mathematical model for multivariate nonlinear prediction of SMD of X-type swirl pressure nozzles," *Process Safety and Environmental Protection*, vol. 125, pp. 228–237, 2019.
- [10] H. Wang, Y. Du, X. Wei, and X. He, "An experimental comparison of the spray performance of typical water-based dust reduction media," *Powder Technology*, vol. 345, pp. 580–588, 2019.
- [11] P. Wang, Y. Shi, L. Zhang, and Y. Li, "Effect of structural parameters on atomization characteristics and dust reduction performance of internal-mixing air-assisted atomizer nozzle," *Process Safety and Environmental Protection*, vol. 128, pp. 316–328, 2019.
- [12] S. Yang, W. Nie, S. Lv et al., "Effects of spraying pressure and installation angle of nozzles on atomization characteristics of external spraying system at a fully-mechanized mining face," *Powder Technology*, vol. 343, pp. 754–764, 2019.
- [13] Q. Liu, W. Nie, Y. Hua, H. Peng, C. Liu, and C. Wei, "Research on tunnel ventilation systems: dust diffusion and pollution behaviour by air curtains based on CFD technology and field measurement," *Building and Environment*, vol. 147, pp. 444–460, 2019.
- [14] H. Wang, W. Nie, W. Cheng, Q. Liu, and H. Jin, "Effects of air volume ratio parameters on air curtain dust suppression in a rock tunnel's fully-mechanized working face," *Advanced Powder Technology*, vol. 29, no. 2, pp. 230–244, 2018.
- [15] S. Li, F. Zhou, F. Wang, and B. Xie, "Application and research of dry-type filtration dust collection technology in large tunnel construction," *Advanced Powder Technology*, vol. 28, no. 12, pp. 3213–3221, 2017.
- [16] G. Xu, Y. Chen, J. Eksteen, and J. Xu, "Surfactant-aided coal dust suppression: a review of evaluation methods and influencing factors," *Science of the Total Environment*, vol. 639, pp. 1060–1076, 2018.
- [17] H. Wang, W. Xuan, Z. Zhang, and B. Qin, "Experimental investigation of the properties of dust suppressants after magnetic-field treatment and mechanism exploration," *Powder Technology*, vol. 342, pp. 149–155, 2019.
- [18] H. Wang, D. Wang, W. Ren, X. Lu, F. Han, and Y. Zhang, "Application of foam to suppress rock dust in a large cross-section rock roadway driven with roadheader," *Advanced Powder Technology*, vol. 24, no. 1, pp. 257–262, 2013.
- [19] H. Wang, X. Wei, Y. Du, and D. Wang, "Experimental investigation on the dilatational interfacial rheology of dust-suppressing foam and its effect on foam performance," *Process Safety and Environmental Protection*, vol. 123, pp. 351–357, 2019.
- [20] H. Wang, X. Wei, Y. Du, and D. Wang, "Effect of water-soluble polymers on the performance of dust-suppression foams: wettability, surface viscosity and stability," *Colloids and Surfaces A: Physicochemical and Engineering Aspects*, vol. 568, pp. 92–98, 2019.
- [21] W. Ren, D. Wang, Q. Guo, and B. Zuo, "Application of foam technology for dust control in underground coal mine," *International Journal of Mining Science and Technology*, vol. 24, no. 1, pp. 13–16, 2014.
- [22] H. Wang, D. Wang, Y. Tang, B. Qin, and H. Xin, "Experimental investigation of the performance of a novel foam generator for dust suppression in underground coal mines," *Advanced Powder Technology*, vol. 25, no. 3, pp. 1053–1059, 2014.
- [23] Q. Wang, D. Wang, H. Wang et al., "Optimization and implementation of a foam system to suppress dust in coal mine excavation face," *Process Safety and Environmental Protection*, vol. 96, pp. 184–190, 2015.
- [24] H. Wang, D. Wang, Y. Tang, and Q. Wang, "Foaming agent self-suction properties of a jet-type foam preparation device used in mine dust suppression," *Process Safety and Environmental Protection*, vol. 98, pp. 231–238, 2015.
- [25] Y. Bartosiewicz, Z. Aidoun, and Y. Mercadier, "Numerical assessment of ejector operation for refrigeration applications based on CFD," *Applied Thermal Engineering*, vol. 26, no. 5–6, pp. 604–612, 2006.
- [26] C. Li and Y. Z. Li, "Investigation of entrainment behavior and characteristics of gas-liquid ejectors based on CFD simulation," *Chemical Engineering Science*, vol. 66, no. 3, pp. 405–416, 2011.
- [27] E. Rusly, L. Aye, W. W. S. Charters, and A. Ooi, "CFD analysis of ejector in combined ejector cooling system," *International Journal of Refrigeration*, vol. 28, no. 7, pp. 1092–1101, 2005.
- [28] Y. Yu, *Introduction and advanced tutorial of FLUENT*, Beijing Institute of Technology Press, Beijing, China, 2008.
- [29] J. D. Anderson, *Computational Fluid Dynamics*, McGraw-Hill, New York, NY, USA, 1995.
- [30] F. J. Wang, *Computational Fluid Dynamics Analysis: Principle and Application of CFD Software*, Tsinghua University Press, Beijing, China, 2004.
- [31] H. Q. Lu, *Jet Technology Theory and Application*, Wuhan University Press, Wuhan, China, 2004.
- [32] R. L. Yadav and A. W. Patwardhan, "Design aspects of ejectors: effects of suction chamber geometry," *Chemical Engineering Science*, vol. 63, no. 15, pp. 3886–3897, 2008.
- [33] I. W. Eames, A. Milazzo, D. Paganini, and M. Livi, "The design, manufacture and testing of a jet-pump chiller for air conditioning and industrial application," *Applied Thermal Engineering*, vol. 58, no. 1–2, pp. 234–240, 2013.
- [34] A. Samad and M. Nizamuddin, "Flow analyses inside jet pumps used for oil wells," *The International Journal of Fluid Machinery and Systems*, vol. 6, no. 1, pp. 1–10, 2013.
- [35] S. Balamurugan, M. D. Lad, V. G. Gaikar, and A. W. Patwardhan, "Hydrodynamics and mass transfer characteristics of gas-liquid ejectors," *Chemical Engineering Journal*, vol. 131, no. 1–3, pp. 83–103, 2007.
- [36] K. Matsuo, Y. Miyazato, and H. Kim, "Shock train and pseudo-shock phenomena in internal gas flows," *Progress in Aerospace Sciences*, vol. 35, no. 1, pp. 33–100, 1999.



**Hindawi**

Submit your manuscripts at  
[www.hindawi.com](http://www.hindawi.com)

